Physics of Fluids

Body-caudal fin fish-inspired self-propulsion study on burst-and-coast and continuous swimming of a hydrofoil model

Cite as: Phys. Fluids **33**, 091905 (2021); https://doi.org/10.1063/5.0061417
Submitted: 26 June 2021 • Accepted: 02 September 2021 • Published Online: 21 September 2021

Siddharth Gupta, Namshad Thekkethil, Amit Agrawal, et al.

Physics of Fluids ARTICLE scitation.org/journal/phf

Body-caudal fin fish-inspired self-propulsion study on burst-and-coast and continuous swimming of a hydrofoil model

Cite as: Phys. Fluids **33**, 091905 (2021); doi: 10.1063/5.0061417
Submitted: 26 June 2021 · Accepted: 2 September 2021 ·
Published Online: 21 September 2021

View Online Export Citation CrossMark

Siddharth Gupta,[1,2,3] Namshad Thekkethil,[1] Amit Agrawal,[1] Kerry Hourigan,[2] Mark C. Thompson,[2] and Atul Sharma[1,a)]

AFFILIATIONS

[1]Department of Mechanical Engineering, Indian Institute of Technology Bombay, Mumbai 400076, India
[2]Fluids Laboratory for Aeronautical and Industrial Research (FLAIR), Department of Mechanical and Aerospace Engineering, Monash University, Melbourne, Victoria 3800, Australia
[3]IITB-Monash Research Academy, IIT Bombay, Mumbai 400076, India

[a)]Author to whom correspondence should be addressed: atulsharma@iitb.ac.in

ABSTRACT

The present study examines the energy efficiency of self-propelled hydrofoils for various modes and kinematics of swimming adopted by various body-caudal fin fish. In particular, this work considers the intermittent burst-and-coast (B&C) and continuous swimming modes, and examines the effect of the undulating and/or pitching swimming kinematics, adopted by the undulating body of anguilliform fish and pitching caudal fin of carangiform and thunniform fish. Notably, B&C swimming is adopted in nature mostly by the latter class but rarely by the former. This fact forms the basis of our study on the hydrodynamics and propulsion performance for both classes of fish-inspired swimming using a NACA0012 hydrofoil model. This analysis explores a large parameter space covering undulation wavelength, $0.8 \leq \lambda^* < \infty$, Reynolds number, $50 \leq Re_f \leq 1500$, and duty cycle (DC), $0.1 \leq DC \leq 1$, with the DC representing the fraction of time in B&C swimming. The fluid–structure dynamics-based vortex-shedding-process is investigated, where B&C swimming results in either an asymmetric reverse von Karman (RVK) or forward von Karman vortex street, rather than a symmetric RVK vortex street observed during continuous swimming. It is demonstrated that the B&C swimming results in an energy saving, although there is a concomitant increase in the travel time. Moreover, our results show that B&C swimming is *effective* for carangiform and thunniform tail-like kinematics but not for anguilliform body-like kinematics of the hydrofoil. Thus, the predictions are consistent with the observed swimming behavior adopted by a fish in nature and provide input into the efficient design of unmanned underwater vehicles.

I. INTRODUCTION

Millions of years of evolution have resulted in biological creatures optimizing their different forms of swimming kinematics. In terms of improving our understanding of how such kinematics leads to an efficient propulsion, it can be challenging to replicate the muscle-induced flexibility-based swimming kinematics seen in different kinds of fish. However, these kinematics are much easier to mimic in the computational fluid dynamics (CFD)-based simulations, which forms the basis of the current study.

About 85% of all fish use oscillations of their body and/or caudal fin (BCF) as their primary mode of propulsion. Such BCF fish are classified into four major categories: anguilliform, sub-carangiform, carangiform, and thunniform,[1,2] with depictions of their body forms shown in Fig. 1. This shows that anguilliform fish possess a slender body shape, whereas carangiform and thunniform fish possess a fusiform body shape along with a pronounced caudal fin/tail, which, in cross-sectional view, is seen to approximate a hydrofoil. The shaded region in the figure shows that, for swimming, anguilliform fish (e.g., eels and lampreys) undulate their whole body, sub-carangiform fish undulate their posterior half, carangiform fish move approximately one-third of their body, and thunniform fish (such as tuna) effectively only move their caudal fin/tail. Thus, the primary mode of swimming kinematics for anguilliform and sub-carangiform fish is body undulation, while it is mainly caudal fin/tail oscillation or pitching for carangiform and thunniform fish.[3]

Beyond the basic kinematics described above, in practice, the different fish categories adopt different strategies to travel through water.

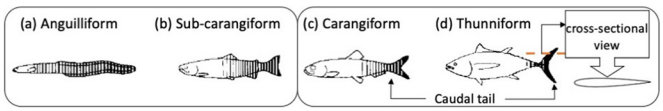

FIG. 1. Different swimming modes of body–caudal fin (BCF) propulsion. The shaded region in the respective fish shows the dominant area used for swimming kinematics, resulting in lateral undulations (with undulation wavelength $\lambda < 1$) of the whole body for fish types (a) and (b), and by the pitching motion (with $\lambda \to \infty$) of the tail (caudal fin) for types (c) and (d). The figure has been adapted from Fig. 5 of Sfakiotakis *et al.*[1]

Burst-and-coast (B&C) swimming[4] is an intermittent two-phase process whereby anguilliform (carangiform) fish undulate (oscillate) their body (tail) during the burst phase and thereafter keep their body (caudal fin) motionless and straight during the coast phase of the cycle. This contrasts to the continuous swimming, which involves employing the burst phase continuously. B&C swimming generates a rapid acceleration during the burst phase and deceleration during the coast phase. *A priori*, this would seem to lead to an energy loss compared with the continuous swimming. However, it has been reported both from numerical and experimental studies that B&C swimming is an efficient energy-saving propulsion mechanism *commonly* observed with the pitching tail of carangiform and thunniform fish,[5–7] but *rarely* found with the undulating body of anguilliform fish.

The non-dimensional parameters that govern the intermittent B&C and continuous motion of a self-propelled fish are as follows: the frequency-based Reynolds number (Re_f); non-dimensional wavelength (λ^*); non-dimensional maximum amplitude at the tail (A_{max}); and duty cycle (DC). The DC is used to describe the degree of intermittency of a swimming fish and can be defined as the ratio of active swimming time T_{burst} to total time, i.e., $T_{Total}(= T_{burst} + T_{coast})$ of swimming. Therefore, $DC = 1$ for a continuous swimmer while $0 < DC < 1$ for an intermittent B&C swimmer. These non-dimensional governing parameters are given as

$$Re_f = \frac{Cfa_{max}}{\nu};\ \lambda^* = \frac{\lambda}{C};\ A_{max} = \frac{a_{max}}{C},$$
$$DC = \frac{T_{burst}}{T_{burst} + T_{coast}}, \tag{1}$$

where ν is the kinematic viscosity of the fluid, C is the chord length of the hydrofoil, a_{max} is the maximum amplitude of hydrofoil at the tail tip, f is the frequency, and λ is the wavelength of the undulating or pitching hydrofoil. Note that the chord length C of the hydrofoil is taken as the length scale l_c, and the velocity scale $v_c = fa_{max}$ is based on the frequency f and maximum amplitude a_{max} of undulation (f).

In the literature, B&C swimming is reported for a range of different circumstances, such as searching a food, chasing, or escaping from other aquatic animals and general locomotion.[8] However, the present survey focuses only on the studies based on the hydrodynamics of B&C swimming and can be categorized into four types: experimental observations on the *hydrodynamics of real fish*, *different theories* discussing the physical reason for energy saving of B&C swimming, various *mathematical models* describing a dominant governing parameter(s) for the B&C swimming, and computational and particle-image velocimetry (PIV) studies based on *B&C using a symmetric hydrofoil*. Previous work in these four categories is presented below.

To observe the *hydrodynamics of real fish* performing B&C swimming, Muller *et al.*[6] conducted PIV experiments on adult and larval zebra Danios fish. They observed that the fish larvae alter their body kinematics and move only posterior parts. Furthermore, they concluded that fish larvae save relatively less energy than fully grown fish in B&C swimming. Similar experimental observations of Koi carp were performed by Wu *et al.*[7] They observed two different modes in the burst phase—a multiple tail-beat (MT) mode and a half tail-beat (HT) mode. They measured the active drag in both burst-and-coast phases and concluded that a fish saves around 45% of its energy when it uses B&C swimming as compared to the continuous swimming. B&C swimming is also reported for schools of fish. Fish *et al.*[9] compared the duration of burst and coast phases for a single fish and a school of fish. They reported that the duration of the burst phase is almost the same in each case. However, the duration of the coast phase is significantly larger for the fish in a school.

Different theories have been suggested by different researchers for energy saving during B&C swimming. Based on the Bone–Lighthill boundary-layer thinning hypothesis, Lighthill[10] compared the results of potential theory (large-amplitude elongated-body theory) with real swimming parameters of a Leuciscus fish provided by Bainbridge.[11] He concluded that the viscous drag on a swimming body is about *four times* that of a gliding body. Based on the muscle efficiency, Rome and Alexander[12] proposed that the ratio of velocity of muscle contraction to maximum velocity of shortening should lie within 0.17–0.36 for efficient performance of fish. If the value falls outside this range, fish switch to B&C swimming for efficiency. Based on a hypothesis that propulsive efficiency of swimming increases with an increase in thrust generation, Iosilevskii[13] proposed a theory that fish alter their thrust generation by using an active burst phase followed by a passive coast phase.

Many *mathematical models* on the B&C swimming of the late 20th century are based on the Bone–Lighthill boundary-layer thinning hypothesis, where the parameter α (defined as the ratio of swimming-body drag to rigid-body drag) was proposed to be the main reason for energy saving. Larger values of α lead to larger savings and, by definition, there are no savings at $\alpha = 1$. Weihs[4] developed a mathematical model and predicted that a fish can save more than 50% of energy by performing B&C swimming. Later, Videler and Weihs[5] combined this model with the kinematics data of cod and saithe fish. For a given α, they observed that energy saving depends on U_f (final velocity after the burst) and U_i (initial velocity before burst). By choosing the optimal values of U_f and U_i, B&C swimming can be 2.5 times more energy efficient than the continuous swimming. Blake[14] developed a hydro-mechanical model to determine the influence of body-shape/fineness ratio (ratio of body length to maximum thickness) on B&C swimming. He proposed that a fish body with a fineness ratio of 5 is most suited to capitalize on the energy advantage of B&C swimming.

One of the earliest numerical simulations of *B&C swimming using symmetric hydrofoils* was performed by Chung.[15] By assuming different symmetric National Advisory Committee for Aeronautics (NACA) hydrofoils as representative of the body shape of a fish, he concluded that a fish can exploit the maximum advantage of B&C swimming by possessing a body shape close to NACA0012 hydrofoil with a fineness ratio of 8.33. However, his result conflicts with that of Blake.[14] Chung[15] also reported the number of shed vortices per cycle of periodic kinematics, as three for B&C swimming but only two for

the continuous swimming of the hydrofoil. More recently, Ehrenstein and Eloy[16] and Ehrenstein *et al.*[17] used the theoretical and computational methods to calculate the increase in skin friction drag on an undulating surface. Their results support the boundary-layer thinning hypothesis. However, the rise in friction drag obtained was only 1.23–1.7 times, relatively small compared to the factor of 4 hypothesized by Lighthill.[10] From these findings, they concluded that the rise in skin friction drag is not the only reason behind the energy savings. Motivated by these results, Akoz and Moored[18] performed inviscid numerical simulations using a teardrop shape hydrofoil performing B&C pitching motion. They proposed fish perform B&C swimming to maintain their reduced frequency and Strouhal number in an optimal range, which results in the desired energy saving. A similar kind of experimental study was presented by Floryan *et al.*[19] In their PIV experiments in a water tunnel, they observed that the individual cycles of B&C swimming are independent of each other. However, both Akoz and Moored[18] and Floryan *et al.*[19] observed four shed vortices shed over a cycle of B&C swimming, in contradiction with that reported by Chung.[15]

The above literature survey reveals four previous experimental[6,7,9,19] and two numerical[15,18] studies on B&C swimming using real fish[6,7,9] and symmetric hydrofoils.[15,18,19] Note that most of these studies on real fish are experimental, while those based on hydrofoils are numerical. Also, the numerical studies reported for B&C swimming are two-dimensional. Finally, these studies on B&C swimming are for the more commonly observed carangiform/thunniform kinematics, while no such studies are available for the rarely observed anguilliform kinematics, where the kinematics mainly corresponds to a smaller λ^*-based body undulation of anguilliform fish and larger λ^*-based pitching-tail of carangiform/thunniform fish. One such exception to B&C swimming in anguilliform fish is for needlefish, which adopt it at higher swimming speeds; however, when they do adopt B&C swimming in preference to continuous swimming, Liao[20] reported that they increase their undulation wavelength, λ^*. Thus, it is interesting to note that body undulation of anguilliform fish used during continuous swimming effectively switches to body-pitching for B&C swimming, approximating the pitching kinematics adopted by the tails of carangiform fish. This suggests that, for the adoption of B&C swimming, the undulation wavelength may be a more critical parameter than the difference in the shape of various BCF fish. Thus, the *first objective* of the present study is to explore the effect of undulation wavelength, λ^*, on B&C swimming performance. This study encompasses the various BCF modes of locomotion, with $\lambda^* < 1$ for the anguilliform fish-like undulations and $\lambda^* \to \infty$ for carangiform/thunniform fish-tail-like pitching motion[21] (see Fig. 1). Furthermore, a NACA0012 hydrofoil is considered here as a generic representative 2 D shape of the body/tail of the various types of BCF fish. Although the number of shed vortices in a cycle of B&C swimming is reported in literature,[15,18,19] the effect of λ^*, DC, and Re_f on the number of shed vortices (which are important for propulsion) is missing. Thus, the *second objective* is to undertake a detailed parametric study into the effect of different non-dimensional governing parameters ($0.8 \leq \lambda^* < \infty$, $0.1 \leq DC \leq 1$, and $50 \leq Re_f \leq 1500$) on the hydrofoil hydrodynamics for B&C compared with the continuous swimming. The range of Re_f considered here is within that considered by Chung[15] in his 2D numerical investigation.

Beyond the above-discussed novelty of studying the effect of λ^*, encompassing both body undulation and tail-pitching kinematics, this study also examines the detailed unsteady vorticity dynamics that correlate the flow physics with the performance parameters for B&C and the continuous swimming. Compared with the previous studies into the energy-saving capability of B&C swimming, here for the first time, we present both advantages and disadvantages of B&C swimming in terms of both energy saving and travel time.

For mimicking BCF fish-like swimming, the present work has two main limitations: first, employing many less-time-consuming but qualitatively representative 2D simulations rather than limited but more realistic 3D simulations; and second, using a hydrofoil-based 2D generalization of the body (tail) of anguilliform (carangiform) fish. The shape of the hydrofoil is similar to that used by Chung[15] and is used here since the top-down projected distribution of a fish tail shows similarities with a symmetric hydrofoil.[22] Even though the present results are based on 2D laminar flow simulations at low Re_f, 2D results have been reported to be qualitatively in agreement (in terms of the basic propulsion mechanism) with the actual 3D turbulent flows generated by (3 D) fish.[23–25] Given this, the present less-time-consuming 2D simulations are capable of providing detailed predictions that help our broader understanding of the complex fluid–structure interaction problem of fish-like locomotion.

II. COMPUTATIONAL METHODOLOGY

A. Unified kinematic model for different types of BCF-inspired swimming

For anguilliform and sub-carangiform fish, the lateral displacement is in the form of a backward-traveling wave over the body. On the other hand, the lateral displacement is in the form of a pitching motion about the caudal tail's leading edge for carangiform and thunniform fish. The general form of these lateral displacements is

$$\Delta Y = A(X)\, Y(X), \tag{2}$$

where $A(X)$ $(= A_{max}X)$ is the non-dimensional amplitude of lateral displacement, $Y(X)$ is the non-dimensional waveform equation, and X $(= x/C)$ is the non-dimensional length measured from the head to the tail of the fish.

For an undulating fish, Videler and Wardle[26] observed that the amplitude of the lateral body displacement increases from just behind the head to the tail tip and the relative amplitude of the tail tip corresponds to approximately 0.1 times the body length. Thus, a linearly increasing amplitude equation, in which the head is stationary and the amplitude of undulation is maximum at the tail tip, with $A_{max} = 0.1$, is used for the present simulations.

In the continuous swimming, as the name suggests, the body undulates continuously. Thus, the duty cycle DC is always equal to one. For the continuous undulation, $Y(X)$ in Eq. (2) is modeled in the literature[27] as

$$Y(X) = \sin\left[2\pi\left(\frac{X}{\lambda^*} - \frac{\tau}{A_{max}}\right)\right]. \tag{3}$$

However, in B&C swimming, the body undulates only during the burst phase, while it remains at rest during its coasting phase. Thus, DC lies in the range $0 < DC < 1$, depending on the burst-to-coast time ratio, as defined in Eq. (1). For these two-phase undulations, $Y(X)$ in Eq. (2) is modeled by Chung[15] as

$$Y(X) = \begin{Bmatrix} 0 & 0 \le X' < \lambda_{bout} - \lambda^* \\ -\frac{1}{2}\left\{1 - \cos\left[\frac{4\pi(X' - \lambda_{bout})}{\lambda^*}\right]\right\} & \lambda_{bout} - \lambda^* \le X' < \lambda_{bout} - \frac{3}{4}\lambda^* \\ -\sin\left[\frac{4\pi(X' - \lambda_{bout})}{\lambda^*}\right] & \lambda_{bout} - \frac{3}{4}\lambda^* \le X' < \lambda_{bout} - \frac{1}{4}\lambda^* \\ \frac{1}{2}\left\{1 - \cos\left[\frac{4\pi(X' - \lambda_{bout})}{\lambda^*}\right]\right\} & \lambda_{bout} - \frac{1}{4}\lambda^* \le X' < \lambda_{bout} \end{Bmatrix}, \quad (4)$$

where $X' = X - \tau/A_{max}$, λ_{bout} is the body wavelength, and λ^* is its undulating part. Note that the definition of DC in Eq. (1) is based on the time period of burst-and-coast phases. However, the above equation for $Y(X)$ does not contain any explicit terms for time T. Thus, similar to Chung,[15] DC is redefined here in terms of λ^* and λ_{bout} by using the relationship between the wave speed (V), wavelength (λ^*), and time (T), i.e., $V = \lambda^*/T$, given as

$$DC = \frac{T_{burst}}{T_{bout/Total}} = \frac{\lambda^*/V}{\lambda_{bout}/V} = \frac{\lambda^*}{\lambda_{bout}}. \quad (5)$$

Thus, in the present simulations, any change in DC of B&C swimming is achieved while maintaining the ratio between λ^* and λ_{bout}. For example, in pure undulation, λ^* is fixed as 0.8, so for a duty cycle of 0.5, λ_{bout} is taken as 1.6.

For a single kinematic equation modeling of both body undulations (performed by the anguilliform and sub-carangiform fish) and caudal fin pitching (by the carangiform and thunniform fish), Thekkethil *et al.*[21,27] proposed a unified kinematic model and showed that the undulation and pitching kinematics can be unified by using a single non-dimensional parameter λ^*. For Eq. (3), they demonstrated that smaller values of λ^* (< 1) correspond to the body undulation, while the larger values ($\lambda^* \to \infty$) are more representative of the pitching motion. This varying λ^*-based unified kinematics model, covering the range of BCF fish, is used in the present self-propelled simulations for both continuous and B&C swimming.

Finally, a constant frequency of unity is used in both continuous and B&C swimming, since Muller *et al.*[6] observed in their experiments that fish and larvae perform single tail flicks during the burst phase of B&C swimming.

B. Computational setup

Figure 2 shows a computational setup for the present physical problem of unsteady flow past an undulating NACA0012 hydrofoil. The figure corresponds to the top/dorsal view for an undulating fish-like body as well as pitching of a caudal fin of a fish—undulating/pitching is in the lateral direction. The model assumes that the fish is neutrally buoyant (i.e., $\rho_f = \rho_w$, where ρ is the density and subscript f and w correspond to fish and water, respectively) and moves in the streamwise direction with no rotational motions. The assumption is justified as the lateral and rotary motions are negligible compared to the stream-wise component.[28,29] The computational domain size, as shown in the figure, is based on the previous relevant studies of our research group on the continuous swimming,[21,27] where a domain-size-independence study was undertaken. It thus seems reasonable to consider the same domain size as appropriate for an investigation into B&C swimming. For the present non-dimensional study, the chord length (C) of the hydrofoil is taken as the length scale and the velocity scale is taken as the product of the non-dimensional maximum amplitude A_{max} and frequency of undulation f. The two lateral sides are marked in the figure as the left side and right side with reference to a fish facing the incoming flow and referred to in later discussions.

Considering the kinematics as undulation/pitching, the computational domain and boundary conditions for the self-propelled simulations are shown in Fig. 2. The figure shows a fixed Cartesian mesh with a non-inertial frame of reference. The foil is considered fixed, and the self-propulsion is implemented by using a timewise varying the stream velocity U_p at the inlet boundary, evaluated from Newton's Second Law of motion at this time step n + 1,[30]

$$U_p^{n+1} = U_p^n + 0.5\frac{\Delta\tau}{A_s}C_T^{net}, \qquad C_T^{net} = \frac{F_T^{net}}{0.5\rho_f u_c^2 C}, \quad (6)$$

where U_p is the non-dimensional propulsion velocity, $\Delta\tau$ is the non-dimensional time step, A_s is the non-dimensional area, and C_T^{net} is the non-dimensional instantaneous thrust force F_T^{net} acting on the hydrofoil. Further, a convective boundary condition with the unit convective velocity (U_c) is used at the outlet. A symmetric boundary condition is used at the left and right boundaries to limit the computational domain in lateral directions. Furthermore, the hydrofoil is considered rigid (no flow-induced deformation) with a no-slip boundary condition at its surface.

III. MATHEMATICAL AND NUMERICAL DETAILS

A. Governing equations

In the non-inertial frame of reference, the fluid dynamics of the present comparative study on B&C and continuous swimming of the

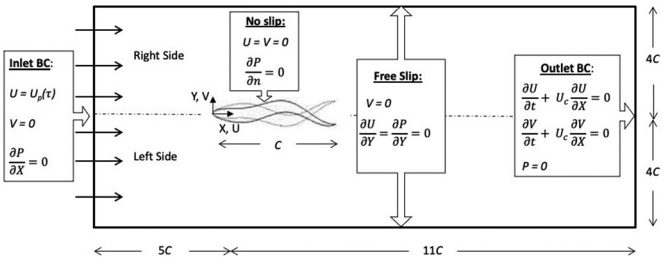

FIG. 2. Non-dimensional computational setup, for the *self-propelled simulations* over a fish-like undulating rigid NACA0012-hydrofoil.

various types of BCF fish is governed by the incompressible Navier–Stokes equations, given as

$$\text{Continuity} : \nabla \cdot \vec{U} = 0, \tag{7}$$

$$\text{Momentum} : \frac{\partial \vec{U}}{\partial \tau} + \nabla \cdot (\vec{U}\vec{U}) = -\nabla P + \frac{1}{Re_f}\nabla^2 \vec{U} + \vec{F}_b, \tag{8}$$

where $\vec{U}$ ($\equiv \vec{U}/u_c$) is the non-dimensional velocity in the non-inertial (accelerating) frame of reference and P ($\equiv p/0.5\rho(A_{max}f)^2$) is the non-dimensional pressure, and $\vec{F_b}$ is the source term that represents the body force vector acting on the non-inertial frame of reference, given as

$$\vec{F_b} = \begin{bmatrix} \frac{du_p}{d\tau} \\ 0 \end{bmatrix}. \tag{9}$$

The coupling of body force with the hydrodynamic forces may lead to instability.[31] Thus, a conservative form of incompressible Navier–Stokes equations is used here. The equations use velocities for the inertial frame of Ref. 32, given as

$$\text{Continuity} : \nabla \cdot \vec{U_i} = 0, \tag{10}$$

$$\text{Momentum} : \frac{\partial \vec{U_i}}{\partial \tau} + \nabla \cdot \left[(\vec{U_i} - \vec{U_R})\vec{U_i}\right] = -\nabla P + \frac{1}{Re_f}\nabla^2 \vec{U_i}, \tag{11}$$

where both $\vec{U_i}$ (fluid velocity) and $\vec{U_R}$ (relative velocity of the fluid) are with respect to the inertial (non-accelerating) frame of reference. Further, $\vec{U_R}$ is given as

$$\vec{U_R} = \begin{bmatrix} -U_p \\ 0 \end{bmatrix}. \tag{12}$$

B. Numerical method

The governing equations presented above are solved by an in-house code that is based on a second-order accurate level-set function-based immersed-interface method (LS-IIM) proposed by Thekkethil and Sharma.[33] The code implements two-dimensional direct numerical simulation, where the temporal variation in the fluid–structure interface is obtained using a level-set function that allows a direct implementation of the interface boundary conditions. The fluid–solid interface is updated at each time step by using the equations of undulation, Eqs. (2)–(4). The in-house code is based on a fully implicit pressure projection method and a collocated grid. It employs the quadratic upstream interpolation for convective kinematics (QUICK) scheme for the advection term and the central-difference scheme for the diffusion term. The in-house code was recently used by Thekkethil *et al.*[27] for self-propulsion simulations; however, they simulated continuous swimming rather than both continuous and B&C swimming simulated in the present work.

C. Code verification and grid independence study

Thekkethil and Sharma[33] presented a detailed verification and validation of the present LS-IIM based in-house code for various one-way and two-way coupled 2D fluid–structure interaction (FSI) problems. Further, Thekkethil *et al.*[27] presented a verification study for self-propulsion simulations of a continuous swimming undulating-hydrofoil. For the present intermittent B&C swimming, the numerical methodology is validated by comparing our results with those of Chung[15] and is shown in Fig. 3(a). The figure shows a good agreement between the present and published results for the time-averaged power $\bar{C}_{P,in}$ and propulsive velocity $\bar{U}_P$ for different Reynolds numbers Re_f and duty cycles DC (marked in brackets) at $\lambda^* = 1$, $f = 1$, and $A_{max} = 0.1$.

A grid independence study is performed here by comparing a temporal variation of instantaneous thrust coefficient C_T^{net} over a non-dimensional period τ, for three Cartesian grid sizes—382×142, 768×314, and 1543×588—at $\lambda^* \to \infty$, $DC = 0.5$, and $Re_f = 1500$ in Fig. 3(b). In each grid, a uniform fine cell size of $\delta = 0.01$, 0.005, and 0.0025 is used in the region enclosing the hydrofoil, and a coarse cell size of $\Delta = 0.5$, 0.25, and 0.125 is used in the far away. A hyperbolic stretching is used to connect the finest and coarsest grid. For $\lambda^* \to \infty$, $DC = 0.5$, $A_{max} = 0.1$, and $Re_f = 1500$, Fig. 3(b) shows no significant difference in C_T^{net} for the two finer grids. Therefore, all further simulations in the present comparative investigation are performed using the intermediate grid size of 768×314, noting that it has 200 points across the hydrofoil chord. This non-uniform Cartesian grid is shown in Fig. 3(c), with the regions marked for the uniform fine grid near the hydrofoil, coarse mesh far away from the hydrofoil, and hyperbolic stretching in the intermediate region.

IV. PARAMETRIC DETAILS

For the present work, the non-dimensional governing input parameters used are shown in Table I. Here, the smaller λ^*-based undulating hydrofoil corresponds to body undulation for an anguilliform/sub-carangiform fish while the larger λ^*-based pitching hydrofoil corresponds to the pitching caudal fin for a carangiform/thunniform fish. The intermediate values of λ^* correspond to hypothetical cases that can fulfill the requirements of the modern-day unmanned autonomous underwater vehicle (AUV). The three values of Reynolds number in the table are chosen such that they correspond to viscous, intermittent, and inertial regimes of the fluid flow, respectively.

The non-dimensional performance parameters, considered in the present study, are as follows:

1. Non-dimensional propulsive velocity U_P (also represented as Re_{up})
2. Thrust coefficient C_T [Eq. (6)]
3. Lateral force coefficient C_L and input power coefficient $C_{P,in}$, given as

$$C_L = \frac{F_L}{0.5\rho_f u_c^2 C}; \quad C_{P,in} = \frac{P_{in}}{0.5\rho_f u_c^3 C} = \frac{\int c_L V_{body} dS}{0.5\rho_f u_c^3 C}, \tag{13}$$

where F_L is the lateral force acting on the hydrofoil, c_L is the local lateral force acting on the hydrofoil per unit surface area, and V_{body} is the local lateral velocity.

Other than the instantaneous value in Eq. (13), a time-averaged value of $\psi = U_P$, C_L, and $C_{P,in}$ is given as

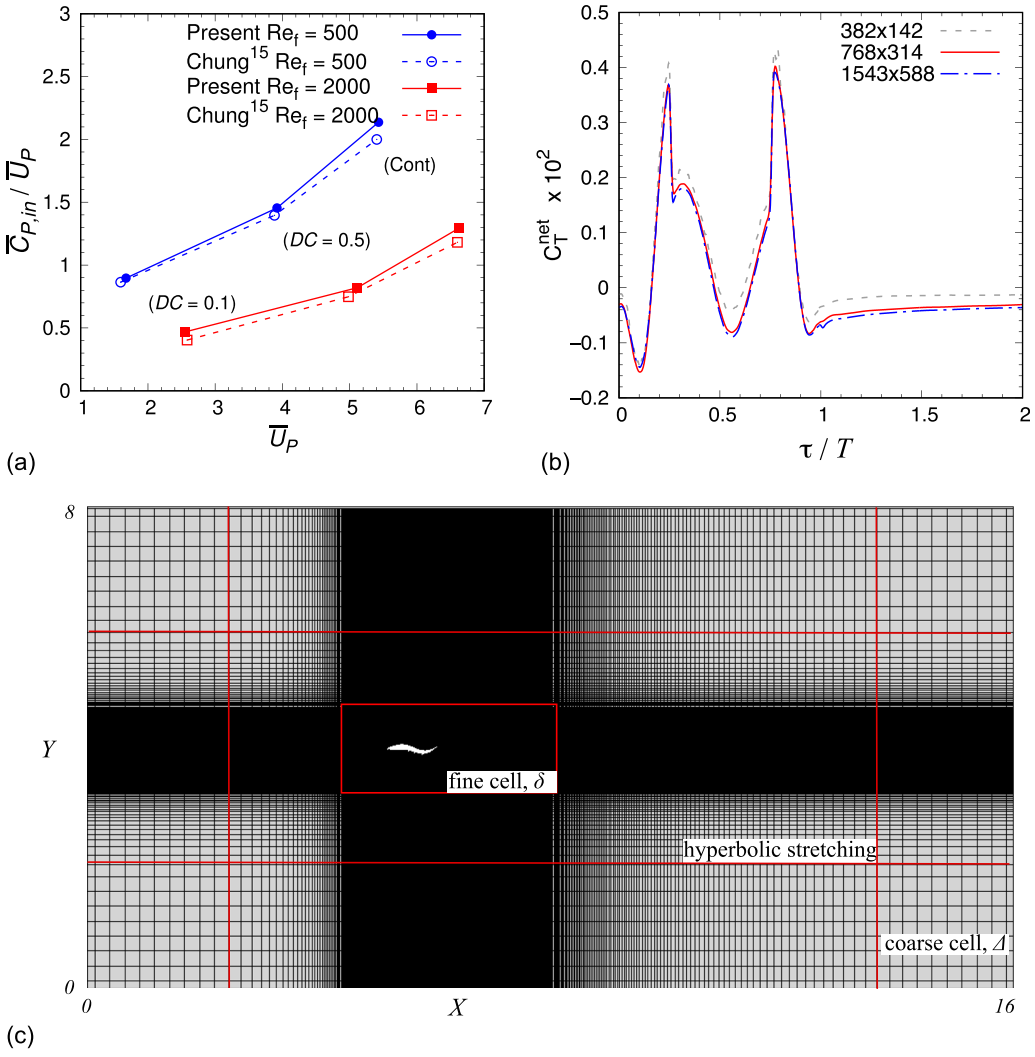

FIG. 3. For a two-dimensional self-propelled NACA0012 hydrofoil, (a) comparison of present and published results (continuous and B&C) for the variation of ratio of time-averaged power $\bar{C}_{P,in}$ and propulsive velocity $\bar{U}_P$ with the increasing $\bar{U}_P$ at $\lambda^* = 1$, $A_{max} = 0.1$, and various DC (marked in brackets) and Re_f; (b) comparison of the temporal variation of instantaneous net thrust coefficient C_T^{net}, for three different grid sizes at the dynamic-steady state for $\lambda^* \to \infty$, $DC = 0.5$, $A_{max} = 0.1$, and $Re_f = 1500$.; and (c) non-uniform Cartesian grid employed for the self-propelled simulations.

TABLE I. Values of the governing parameters for the present numerical study, where all λ^* values below are considered for $DC = 0.5$ and 1, while all the DC values are considered for $\lambda^* = 0.8, 1.8$, and ∞ only.

Non-dimensional input parameters	Symbol	Parametric range
Non-dimensional wavelength	λ^*	0.8, 1, 1.2, 1.5, 1.8, 2.2, 2.8, 3.4, 4, 5, 6, 7, 8, and ∞
Duty cycle	DC	0.1, 0.25, 0.5, 0.75, and 1
Reynolds number	Re_f	50, 500, 1500
Non-dimensional maximum amplitude at the tail tip	A_{max}	0.1

$$\bar{\psi} = \int_0^{2T} \psi d\tau / 2T, \tag{14}$$

where the cycle-wise average value corresponds to two cycles for continuous swimming and one cycle for burst-and-coast phase of intermittent B&C swimming.

V. SELF-PROPULSION CHARACTERSTICS

After the onset of the continuous and the intermittent (B&C) swimming, the effect of the chord-wise flexibility λ^* on the cycle-wise (two-cycle for the continuous swimming and one-cycle each for the burst and coast phase of the intermittent swimming) time-averaged parameters is shown in Fig. 4. For the self-propulsion characteristics of the hydrofoil, the figure shows a cycle-wise variation of mean thrust coefficient $\bar{C}_T$, mean propulsion velocity $\bar{U}_P$, and mean input power coefficient $\bar{C}_{P,in}$.

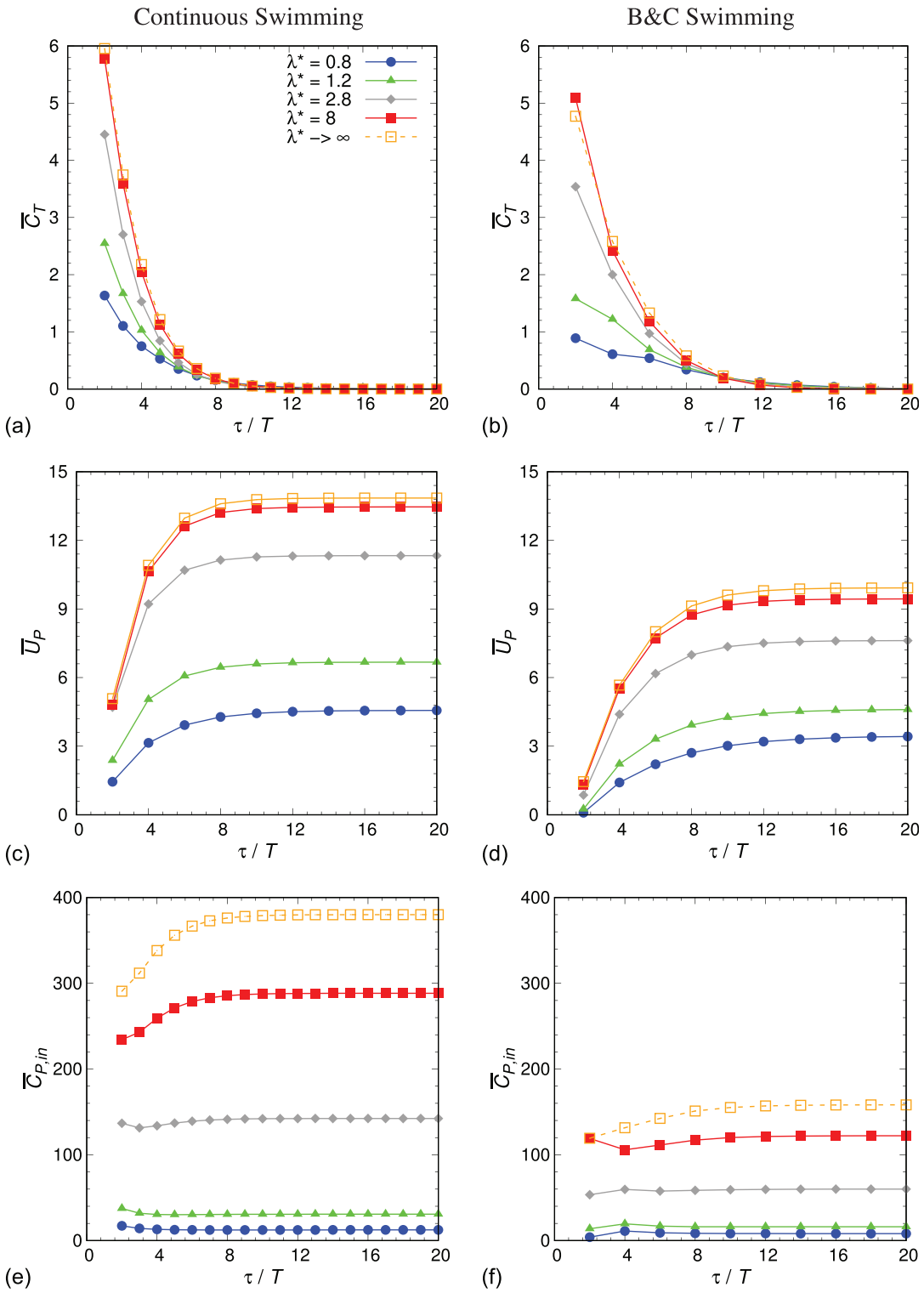

FIG. 4. Cycle-wise variation of the time-averaged values [Eq. (14)] of (a and b) thrust coefficient $\bar{C}_T$, (c and d) propulsive velocity $\bar{U}_P$, and (e and f) input power coefficient $\bar{C}_{P,in}$ for [(a), (c), (e)] continuous and [(b), (d), (f)] B&C swimming at $DC = 0.5$ and $Re_f = 500$. The symbol T on the x axis represents the non-dimensional time-period and τ is the non-dimensional time.

For both continuous and intermittent swimming, after the onset of the periodic-motion of the hydrofoil, Figs. 4(a) and 4(b) show an asymptotic decrease in the mean thrust coefficient $\bar{C}_T$. The associated asymptotic decrease in the acceleration of the hydrofoil results in an asymptotic increase in the propulsive velocity $\bar{U}_P$, as seen in Figs. 4(c) and 4(d). As expected, the figures show that $\bar{U}_P$ approaches a constant value when $\bar{C}_T$ approaches the asymptotic zero value corresponding to the flow approaching a periodic state. At the periodic state, Figs. 4(c)–4(f) show that the asymptotic constant values of both $\bar{U}_P$ and mean input power $\bar{C}_{P,in}$ increase with the increasing λ^* for both types of swimming. An increasing λ^* corresponds to a decreasing muscle-induced flexibility, leading to the transition from undulating to pitching motion as per the unified kinematics model used here. At a constant λ^*, the figure shows a smaller asymptotic value of $\bar{U}_P$ as well as $\bar{C}_{P,in}$ for the B&C as compared to the continuous swimming. However, it is interesting to note from the figure that for intermittent swimming, the reduction is more substantial for the mean input power $\bar{C}_{P,in}$ than the reduction in the mean propulsive velocity $\bar{U}_P$. Referring to the asymptotic values of $\bar{C}_{P,in}$ and $\bar{U}_P$ in the figure for pitching hydrofoil ($\lambda^* \to \infty$), the reduction for the B&C as compared to continuous swimming is 58.4% for $\bar{C}_{P,in}$ and 28.3% for $\bar{U}_P$.

VI. ANALYSIS OF VORTEX-SHEDDING DYNAMICS BEHIND A PITCHING/UNDULATING HYDROFOIL: CONTINUOUS vs BURST-AND-COAST SWIMMING

Eaton[34] presented an analysis of a laminar vortex shedding process behind a stationary circular cylinder by computer-aided flow visualization of temporal variation of streamlines. Such a detailed analysis is not available in the literature for the present FSI problem, especially for the B&C swimming, and is attempted here with the help of temporal variation of vorticity contours in the near wake.

For continuous swimming, Thekkethil *et al.*[21] correlated a time-wise variation of the structural dynamics and the vorticity dynamics. They presented a structural kinematics-driven description of the process of vortex-shedding for the unified kinematic model-based undulating hydrofoil, where $\lambda^* \to \infty$ corresponds to a pitching hydrofoil. Also described was the temporal variation of the structure-driven vortical events of a particular clockwise (CW) and counterclockwise (CCW) vortex. For a CW/CCW vortex, they defined a sequence of instantaneous kinematics states: *stopping vortex* $V_{stop}^{CW/CCW}$, *starting vortex* $V_{start}^{CW/CCW}$ and *shed vortex* $V_{shed}^{CW/CCW}$. This approach for the continuous swimming is continued here for B&C swimming, and the kinematics-driven vortex-shedding process for both the types of swimming are compared in the present work.

A. Structural kinematics-driven vortex–hydrofoil interaction dynamics: Stopping, starting, stretching, and shed CW/CCW vortices

A vortex–hydrofoil interaction dynamics-based sequence of vortical events during the vorticity dynamics—corresponding to a stopping, starting, stretching as well as advecting, and finally, shedding of the CW/CCW vortices—are presented in Figs. 5 and 6. The figures correspond to an undulating ($\lambda^* = 0.8$) hydrofoil and show the periodic vorticity dynamics for both continuous and B&C swimming.

For the continuous swimming, when the foil approaches the leftmost position (refer Fig. 2 for the definition of left and right side)

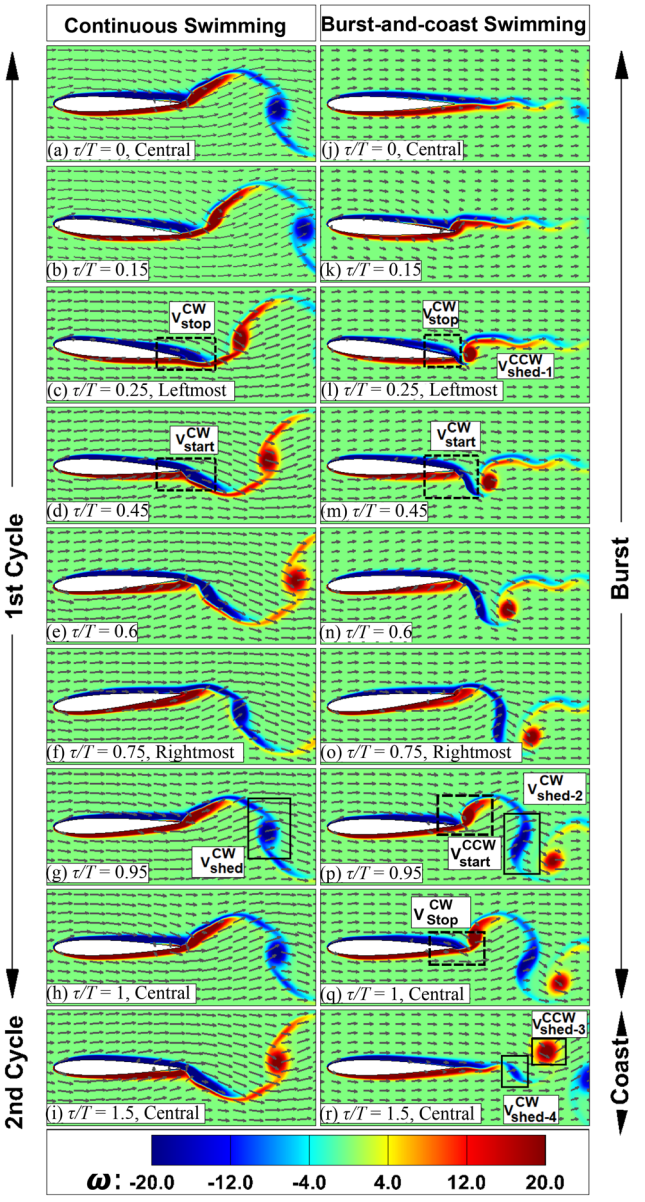

FIG. 5. Temporal variation in instantaneous vorticity contours along with the velocity vectors within two time periods of a pitching ($\lambda^* \to \infty$) hydrofoil performing (a)–(i) continuous and (j)–(r) B&C at $A_{max} = 0.1$ and $Re_f = 500$.

during the pendulum-like pitching motion of the hydrofoil, Thekkethil *et al.*[21] called the growing CW vortex on the right side of the foil [refer to Figs. 5(a)–5(c)] a stopping-vortex V_{stop}^{CW} at a time-instant corresponding to the momentarily stopping of its leftward movement. Thereafter, when the foil reverses its direction (to rightward), the V_{stop}^{CW} is then called a starting vortex V_{start}^{CW} [marked in Fig. 5(d)], which gets stretched and advected downstream during the rightward sweep of the foil [refer Figs. 5(c)–5(f)]. Finally, when the

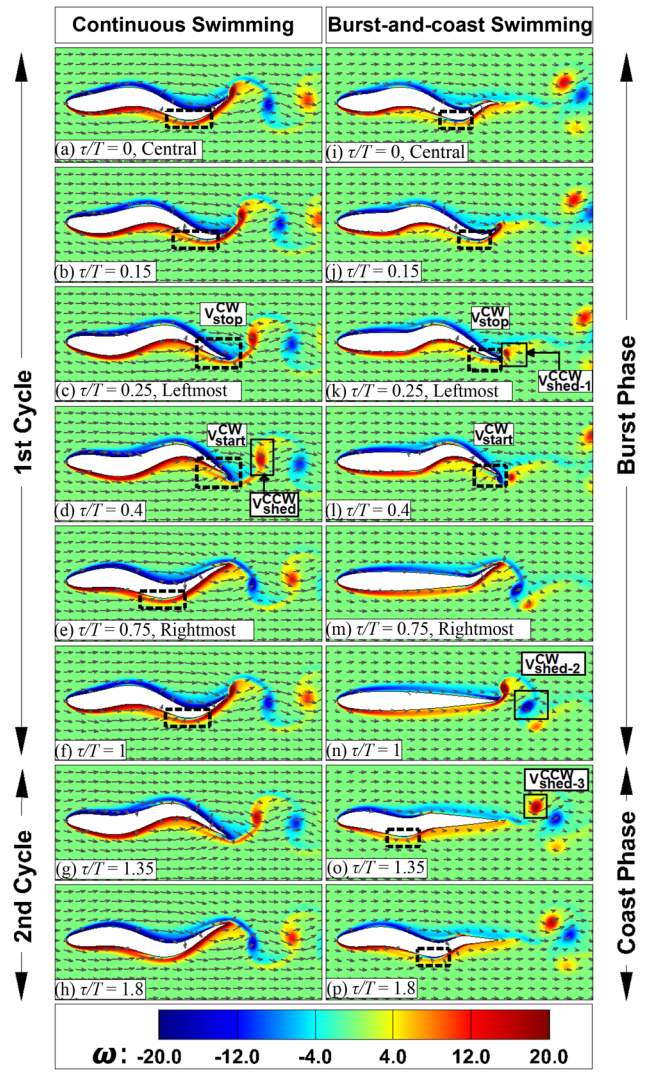

FIG. 6. Temporal variation in the periodic vortex structure along with velocity vectors for one time period of a hydrofoil performing continuous [(a)–(h)] and B&C [(i)–(p)] undulation motion ($\lambda^* = 0.8$) at $A_{max} = 0.1$, and $Re_f = 500$.

foil further reverses its direction (rightward to leftward), the reversal initiates a break-off of the V^{CW}_{start}, which sheds before the foil reaches its central position—this vortex is called a CW shedding vortex V^{CW}_{shed} [shown marked in Fig. 5(g)].

For the B&C swimming of a pitching hydrofoil at $DC = 0.5$, the stretching and downstream advection of the V^{CW}_{start} during the rightward sweep of the hydrofoil are seen in Figs. 5(m)–5(o). The V^{CW}_{start} sheds after the reversed leftward motion, marked as V^{CW}_{shed-2} in Fig. 5(p). However, since the leftward sweep halts at the intermittent central location due to the transition from the burst to the coast phase, the stretching and the advection of the CCW vortex V^{CCW}_{start} get curtailed [Figs. 5(o)–5(q)], and it sheds later [marked as V^{CCW}_{shed-3} in Fig. 5(r)] in the coast phase. The growth of the CW vortex on the right side also gets curtailed, and it stops at the central location [marked as V^{CW}_{stop} in Fig. 5(q)]. The V^{CW}_{stop} does not undergo the kinematics-driven stretching (as the hydrofoil is stationary in the coast phase) and sheds later in the coast phase as a weak CW shed vortex-4, marked as V^{CW}_{shed-4} in Fig. 5(r). Further, the stretching and streamwise advection of another CCW vortex are seen in Figs. 5(j) and 5(k) at the beginning of the burst phase that sheds-off almost when the hydrofoil reverses its direction (from leftward to rightward) as seen in Fig. 5(l), marked as V^{CCW}_{shed-1}. Thus, two pairs (CW-CCW) of vortices are shed: one pair in the burst phase and the other in the coast phase of the B&C swimming cycle. The shed vortices are marked in Figs. 5(j)–5(r) as V^{CCW}_{shed-1} and V^{CW}_{shed-2} for the burst phase and V^{CCW}_{shed-3} and V^{CW}_{shed-4} for the coast phase. The numbering of these vortices is chronologically arranged as per the sequence of their shedding. The above-presented number of vortices shed in a cycle of B&C swimming of a pitching hydrofoil matches the experimental observation of Floryan *et al.*[19] and the numerical results of Akoz and Moored.[18]

Note from Figs. 5(d)–5(i) that the center of V^{CW}_{shed} and V^{CCW}_{shed}, generated on the right and (left) surface of the hydrofoil, is located almost at the leftmost (rightmost) location of the hydrofoil. Similarly located V^{CW}_{shed-2} and V^{CCW}_{shed-3} can be seen in Figs. 5(j)–5(l) for the B&C swimming. In contrast, the center of V^{CCW}_{shed-1} is seen near the leftmost and the center of V^{CW}_{shed-4} is near the central location. Thus, V^{CW}_{shed-2} and V^{CCW}_{shed-3} form a *reverse* von Karman street while V^{CW}_{shed-4} and V^{CCW}_{shed-1} form a leftward inclined *forward* von Karman street in the far wake, as shown and discussed in Sec. VI B.

Figure 6 shows the vortex shedding process for an undulating hydrofoil ($\lambda^* = 0.8$) for both the types of swimming. For the continuous swimming, a rectangular marked region in Figs. 6(e) and 6(f) and 6(a) and 6(b) shows a growth (on the left surface) of a small-sized CW vortex and its downstream advection along the chord before it merges with a same signed stopping vortex V^{CW}_{stop} (on the right surface) in Fig. 6(c). Thekkethil *et al.*[21] called this small-sized vortex on the opposite side as a *secondary vortex* V_{sec} and presented it as a signature for the thrust generation.

For the B&C swimming of an undulating hydrofoil at $DC = 0.5$, similar growth and posterior travel of the V^{CW}_{sec} can be seen within the marked rectangular region in Figs. 6(o), 6(p), 6(i), and 6(j) before it merges with the same-signed stopping vortex V^{CW}_{stop} when the tail tip reaches its leftmost position in Fig. 6(k). Thereafter, a change in the leftward-to-rightward undulation leads to the immediate shedding of V^{CCW}_{shed-1} almost at the leftmost tail position [Fig. 6(k)], which is different from the continuous swimming where the V^{CCW}_{shed} sheds close to the hydrofoil centerline [Fig. 6(d)]. Later in the coast phase, Figs. 6(n)–6(p) shows the shedding of a CCW vortex V^{CCW}_{shed-3} but not that of a V^{CW}_{shed-4}, in contrast to that seen in Fig. 5(r) for the pitching hydrofoil. Thus, in the coast phase, the undulations lead to only one shed vortex as compared with the pair of shed vortices for the pitching hydrofoil. This leads to three shed vortices (2 CCW and 1 CW) for the undulating hydrofoil compared with four shed vortices (2 CCW and 2 CW) for the pitching hydrofoil, within a B&C cycle. The number of shed vortices for an undulating hydrofoil, reported here, matches with the numerical results of Chung.[15]

B. Direction of the advecting starting vortex until it sheds

For the continuous swimming of a pitching foil, Thekkethil *et al.*[21] demonstrated that the advection of the center of the stretching starting vortex is almost horizontal, i.e., the center of the V_{start}^{CW} remains almost at the same leftmost position of the foil, corresponding to the center of the V_{stop}^{CW}, while it is stretching as well as advecting downstream during the left-to-right motion as seen in Figs. 5(c)–5(f). This leads to the shedding of CW (CCW) vortex at the leftmost (rightmost) position of the hydrofoil, as seen in Fig. 5(g) [Fig. 5(d)], and formation of a reverse von Karman street. However, for an undulating hydrofoil, they showed that the streamwise traveling wave over the foil leads to a slightly inclined (toward the centerline) advection of the V_{start}^{CW}, as seen in Figs. 6(c)–6(e), and a reduction in the transverse distance between the CW-CCW shed vortices of the reverse von Karman street.

For the other case of B&C swimming with regard to the start vortices, Figs. 5(j)–5(r) and Figs. 6(i)–6(p) show similarly advecting $V_{start-2}^{CW}$ and $V_{start-3}^{CCW}$. However, the advection process as well as its direction is quite different for $V_{start-1}^{CCW}$ and $V_{start-4}^{CW}$ in the B&C swimming. The difference is due to the coast phase that introduced the intermittent stopping compared with a momentarily stop in the continuous swimming. Figures 5(j)–5(l) and 6(i)–6(k) show that $V_{start-1}^{CCW}$ at the central position of the tail tip advects in the leftward inclined direction driven by the onset of burst phase-based leftward kinematics of the hydrofoil and sheds at the leftmost position. The leftward inclined advection is seen for both pitching and undulating B&C swimming. However, this inclined advection is *outward* from the centerline for the B&C swimming as compared to inward for the continuous swimming of the undulating hydrofoil. For $V_{start-4}^{CW}$, Fig. 5(r) for the pitching foil shows that the formation, advection, and shedding occur horizontally along the central position in contrast to the continuous swimming, where the horizontal advection occurs at the leftmost/rightmost position.

A schematic representation of the structure kinematics-driven vortex shedding process is shown in Fig. 7. For the continuous swimming of a pitching foil, Fig. 7(a) shows horizontal advection of V_{shed}^{CW} at the leftmost position and that of V_{shed}^{CCW} at the rightmost position. For a B&C pitching hydrofoil, Fig. 7(a) shows similar results for V_{shed-2}^{CW} and V_{shed-3}^{CCW} while V_{shed-4}^{CW} advects horizontally at the central position and $V_{start-1}^{CCW}$ advects leftward. For a continuous undulating hydrofoil, Fig. 7(b) shows a centrally inclined advection of $V_{start}^{CW/CCW}$ that results in the shed vortex $V_{shed}^{CW/CCW}$ closer to the centerline as compared to that for the continuous pitching hydrofoil. For the B&C swimming undulating hydrofoil, similar results are seen in Fig. 7(b) for V_{shed-2}^{CW} and V_{shed-1}^{CCW}, while a leftward advection is seen for $V_{start-1}^{CCW}$.

The above-discussed direction of the advection of the vortices in the rear wake is important since it decides the transverse distance between the shed vortices in the far wake. As presented below, a reverse von Karman street is formed in the far wake for the *continuous* swimming where the transverse distance is larger for the pitching hydrofoil and smaller for the undulating hydrofoil, which leads to a larger and smaller thrust force as well as propulsive velocity for the respective hydrofoils. Moreover, for B&C as compared to continuous swimming, a forward von Karman street is also formed (presented below) that leads to a decrease in the thrust force as well as propulsive velocity.

VII. CHARACTERIZATION OF INSTANTANEOUS VORTEX-STREET

For the continuous and B&C swimming, the above-discussed difference in the vortex shedding process in the near wake results in a

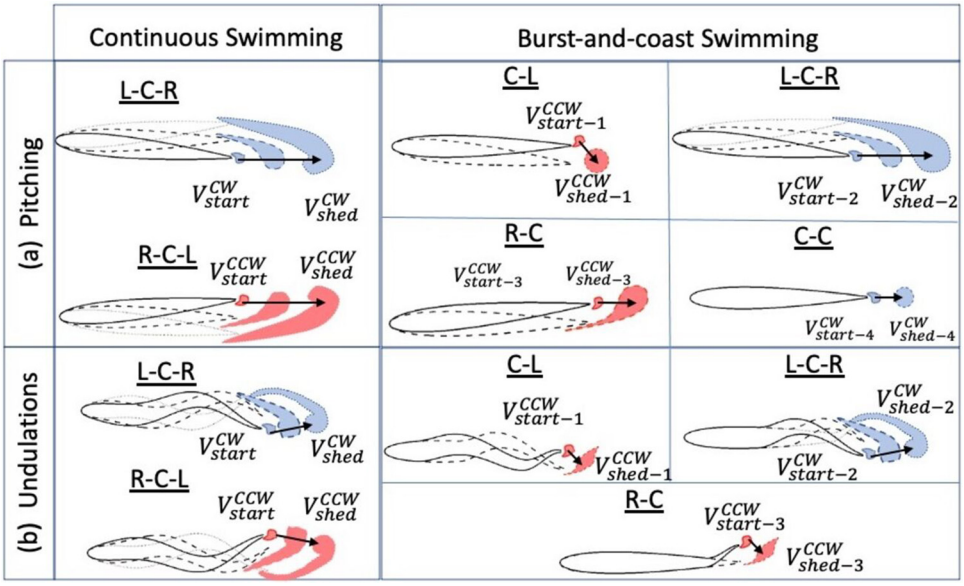

FIG. 7. Schematic representation of the horizontal and inclined advection of the stretching starting vortex V_{start} for both continuous and B&C swimming of (a) pitching and (b) undulating hydrofoil. The timewise sequence of positions of the hydrofoil and the starting vortex is represented by solid, dashed, and dotted lines where L-C-R represents leftmost to central to rightmost motion of the hydrofoil. The advection of the V_{start} is represented by thick black arrow.

different vortex street pattern in the far wake. This is shown in Fig. 8 with the help of instantaneous vortex structures for the two types of swimming. Furthermore, for the B&C swimming, Figs. 9–11 show the downstream evolution of the vortex structure under the effect of λ^*, Re, DC, respectively, presented in a separate subsection below. The time instant for the instantaneous vorticity contours corresponds to the central position of the tail for the continuous swimming and end of the coast phase for the B&C swimming. These figures also show a streamwise variation of the maximum magnitude of instantaneous vorticity of the CW and CCW shed vortices.

Figure 8(a) shows a symmetric reverse von Karman (RVK) street for the continuous swimming, while Fig. 8(b) shows both RVK and forward von Karman (FVK) vortex streets for the B&C swimming. As discussed above, the RVK street is formed by V^{CW}_{shed-2} and V^{CCW}_{shed-3}, and the FVK street is formed further downstream by V^{CCW}_{shed-1} and V^{CW}_{shed-4}. Further, it can be seen from Fig. 8(b) that both the forward and reverse vortex streets are asymmetric and deviate laterally from their mean path of motion—RVK is rightward while FVK is leftward from the centerline.

The rightward or leftward deviation is due to a much smaller spacing between the shed vortices, called as a dipole,[27] that leads to an induced rightward or leftward jet flow in between the oppositely signed vortex pair. The process of formation of these dipoles is discussed here using a schematic plot in Fig. 8(c). The figure shows that

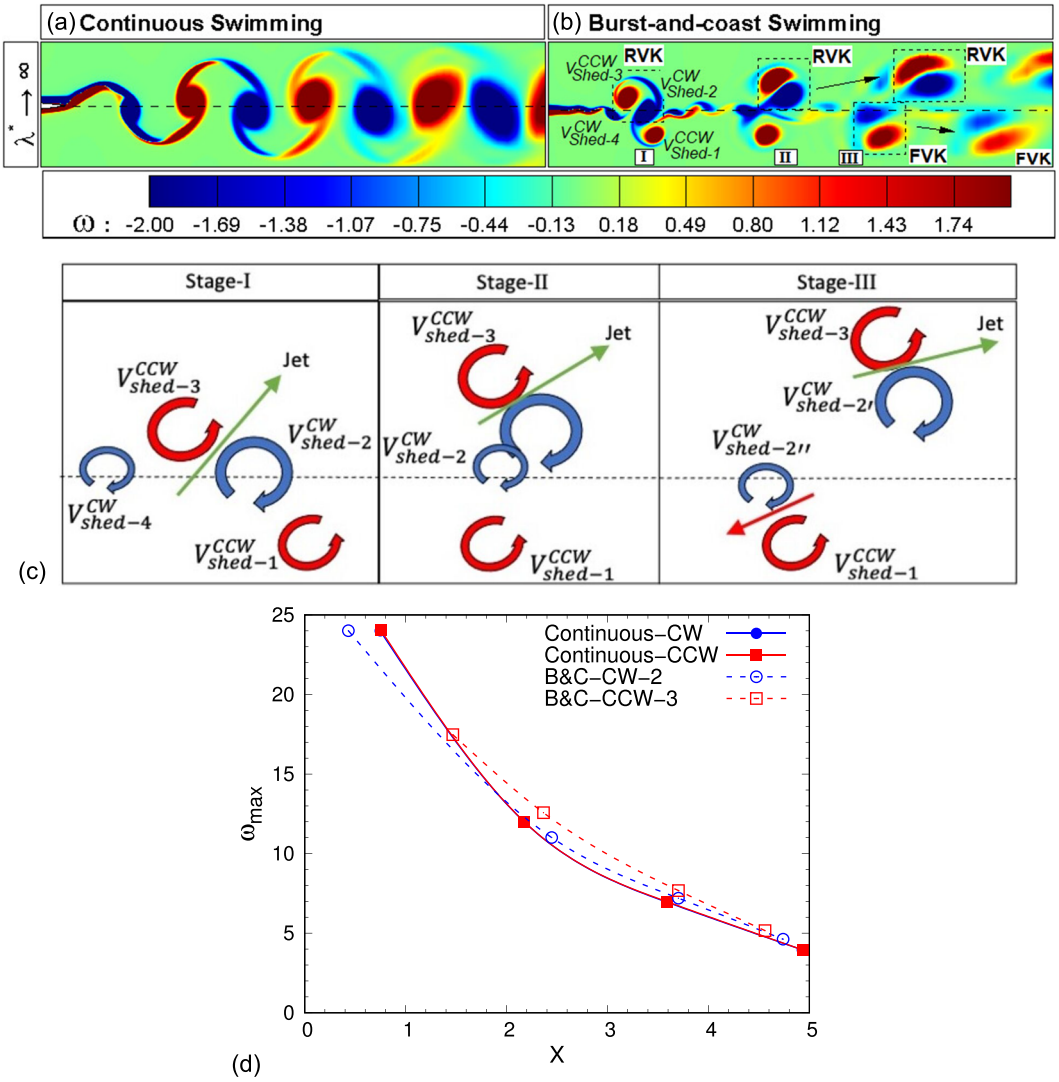

FIG. 8. Comparison of the (a and b) vorticity contour-based vortex street with (d) streamwise variation (from the tail tip) of maximum instantaneous vorticity for the continuous and B&C swimming of a pitching hydrofoil at $A_{max} = 0.1$ and $Re_f = 500$. For the B&C swimming, a schematic representation of the downstream evolution of the vortex structure is presented in (c) in terms of three stages: Stage-I on formation of a dipole-based RVK street, Stage-II on merging of CW vortices, and Stage-III on the binary breakup of the merged CW vortex as well as the formation of asymmetric RVK and FVK vortex streets [also shown marked in (b)]. The adjoining opposite-sign shed vortices are marked by a straight arrow in (d).

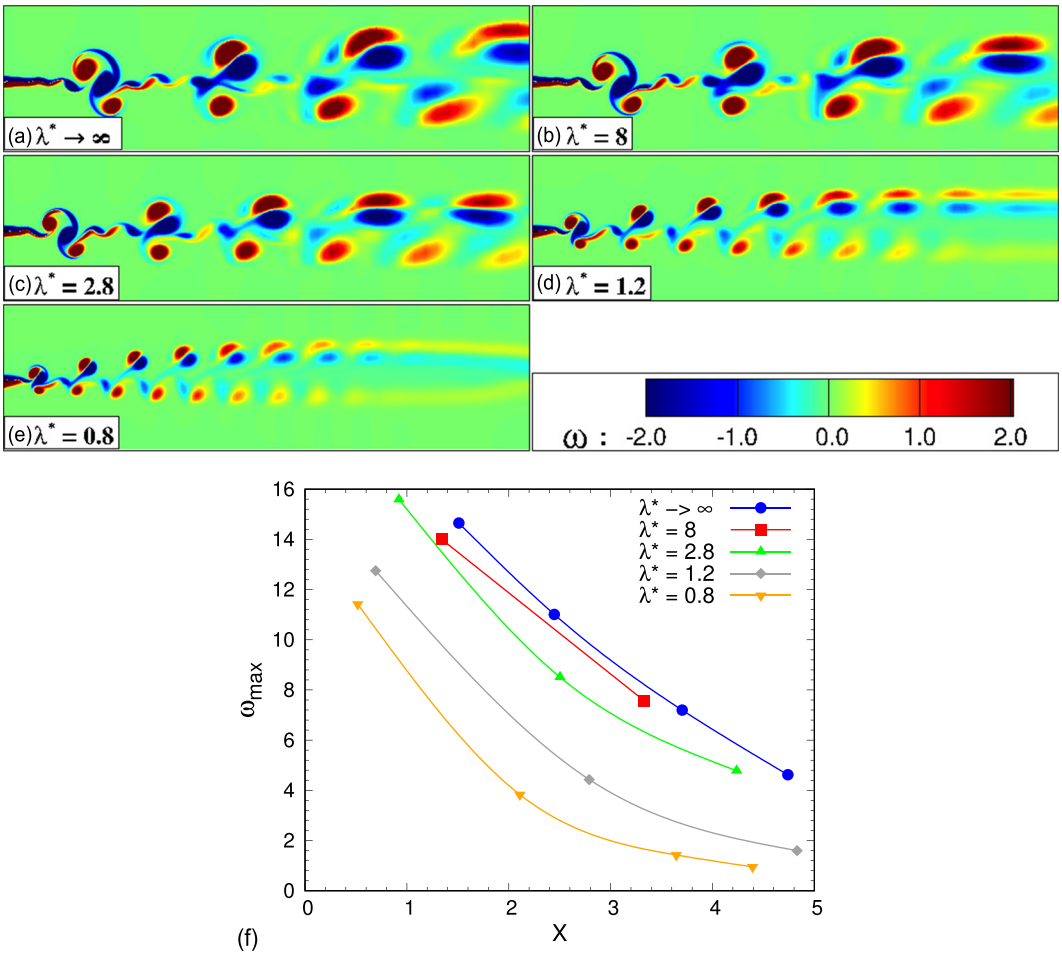

FIG. 9. For B&C swimming at $DC = 0.5$, $A_{max} = 0.1$, and $Re_f = 500$, the effect of chordwise flexibility λ^* on an instantaneous (a)–(e) vorticity contour and (f) streamwise variation of maximum vorticity ω_{max} of the shed vortex V^{CW}_{shed-2}.

the formation of RVK and FVK streets can be divided into three stages. In Stage-I, the centers of V^{CW}_{shed-2} and V^{CCW}_{shed-3} are located at the central and rightmost location of the hydrofoil, respectively. Note from Fig. 5(b) that the center of V^{CW}_{shed-2} was at the leftmost location when it shed from the tail tip and it moved in a rightward direction after it is shed during the burst phase and approaches the center by the end of the consecutive coast phase [Fig. 8(b)]. This lateral movement brings the oppositely signed and almost equal strength vortices (V^{CW}_{shed-2} and V^{CCW}_{shed-3}) closer, forming a dipole-based RVK street in stage-I. This vortex street induces the surrounding fluid and forms a momentum surplus rightward jet required for the propulsion [shown marked by the arrow in Fig. 8(c)]. A rightward movement of the RVK vortex pair and a surplus jet are seen in the figure for stage-II, leading to the merging of V^{CW}_{shed-4} with V^{CW}_{shed-2}. However, the merged CW vortex quickly separates into two, $V^{CW}_{shed-2'}$ and $V^{CW}_{shed-2''}$, in Stage-II. The larger vortex $V^{CW}_{shed-2'}$ continues to move downstream as a dipole-based RVK. In contrast, the smaller $V^{CW}_{shed-2''}$ approaches V^{CCW}_{shed-1}, resulting in a weak dipole-based FVK vortex street in the far wake in Stage-III. In contrast to the momentum-excess wake created by the dipole-based RVK, the dipole-based FVK street creates a momentum deficit wake. Note that the leftward deviation of the FVK vortex street is smaller compared with the rightward deviation of the dipole-based RVK street due to the weaker vortex pair in the FVK as compared to the RVK vortex street.

The instantaneous vorticity contour plots of Figs. 8(a) and 8(b) also shows a difference in the shape of shed vortices for the two types of swimming. The shape of the shed vortices is elliptical with a strong braid region for the continuous swimming whereas the shape for the B&C swimming is close to circular with negligible braid region (except for the V^{CW}_{shed-2}). The difference in shapes is due to the difference in the stretching of the vortices in the two types of swimming, as discussed in Sec. VI A. Despite the difference in the shape of the shed vortices for the two types of swimming, Fig. 8(d) shows that the magnitude of maximum instantaneous vorticity of the RVK shed vortices is almost the same, and the vortices dissipate similarly while traveling downstream in the wake for the two types of swimming. However, the shed vortices are symmetrical for continuous swimming, while they are asymmetrical for B&C swimming.

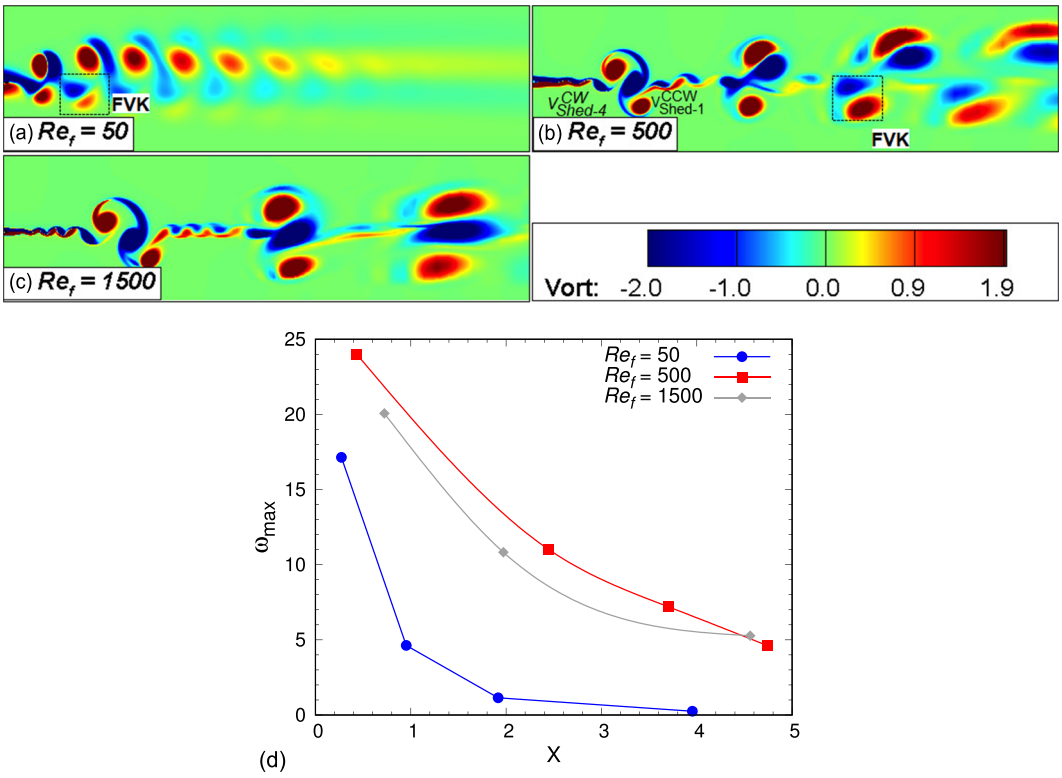

FIG. 10. For B&C swimming of a pitching hydrofoil ($\lambda^* \to \infty$) at $DC = 0.5$, and $A_{max} = 0.1$, the effect of Re_f on an instantaneous (a)–(c) vorticity contour and (d) streamwise variation of maximum vorticity ω_{max} of the shed vortex V^{CW}_{shed-2}.

A. Effect of muscle-induced chord-wise flexibility

The effect of muscle-induced chord-wise flexibility—associated with non-dimensional wavelength of undulation $\lambda^*(= 0.8–\infty)$—on the instantaneous vortex structures for the B&C swimming is shown in Figs. 9(a)–9(e). The figure shows that the size of the shed vortices decreases with the decreasing λ^*, which corresponds to the transition from pure pitching to the various types of undulation. Furthermore, with the decreasing λ^*, Fig. 9(f) shows a decrease in the magnitude of maximum instantaneous vorticity of shed vortices. The consequence of this decrease in the size and the strength of the shed vortices can be seen in the number of observable shed vortices in Figs. 9(a)–9(e), which is four in B&C cycle for pitching and reduces to three for $\lambda^* < 1.8$. For the B&C swimming, the four shed vortices was reported by Akoz and Moored[18] and Floryan *et al.*[19] for pitching; and Chung[15] reported three shed vortices for undulating hydrofoil.

For the RVK street, Figs. 9(a)–9(e) show that the streamwise spacing between two consecutive pair of shed vortices decreases while their rightward deviation increases with the decreasing λ^*. The larger rightward deviation is due to the formation of a dipole in the wake at a shorter streamwise distance from the tail tip with decreasing λ^*. Note the larger deviation of vortices from the mean central line in the wake results in a large C_L-based larger input power $C_{P,in}$. This results in the decrement in the propulsive performance of B&C swimming while undulating at smaller chordwise flexibility, discussed below in Sec. VIII.

B. Effect of Reynolds number

For a pitching hydrofoil performing B&C swimming, Fig. 10 shows the effect of Reynolds number Re_f on the instantaneous vortex street for three different flow regimes—viscous, transitional, and inertial at $Re_f = 50, 500$, and 1500, respectively. The figure shows that the dipole-based FVK vortex street forms adjacent to the tail tip at $Re_f = 50$, forms in the far wake at $Re_f = 500$, and does not form at $Re_f = 1500$. The delay in the formation of the dipole-based FVK street and its disappearance with the increasing Re_f are due to the associated increase in the inertia of the flow that results in a faster downstream travel of vortex V^{CCW}_{shed-1}. Thus, the time required or the downstream distance required for V^{CW}_{shed-4} to approach vortex V^{CCW}_{shed-1} increases. At the larger $Re_f = 1500$ studied here, the merged CW vortices do not split into two, as occurs in Stage-III for $Re_f = 500$ discussed above [Fig. 8(d)]. Thus, for $Re_f = 1500$, the observable shed vortices reduce to three even for the pitching hydrofoil with B&C swimming. The present result matches with the experimentally observed result of Wu *et al.*[7] of three vortices in the wake of real koi carp fish performing B&C swimming. Note that the koi carp is a carangiform type of fish, and the experiments were carried out at $Re_f \approx 2600$. Further, the spatial distribution of the vortices in the wake from the present numerical simulations matches the experimental observations on a real koi carp fish by Wu *et al.*[7]

Figures 10(a)–10(c) also show that the rightward deviation of vortices in the street decreases with the increasing Re_f. This indicates

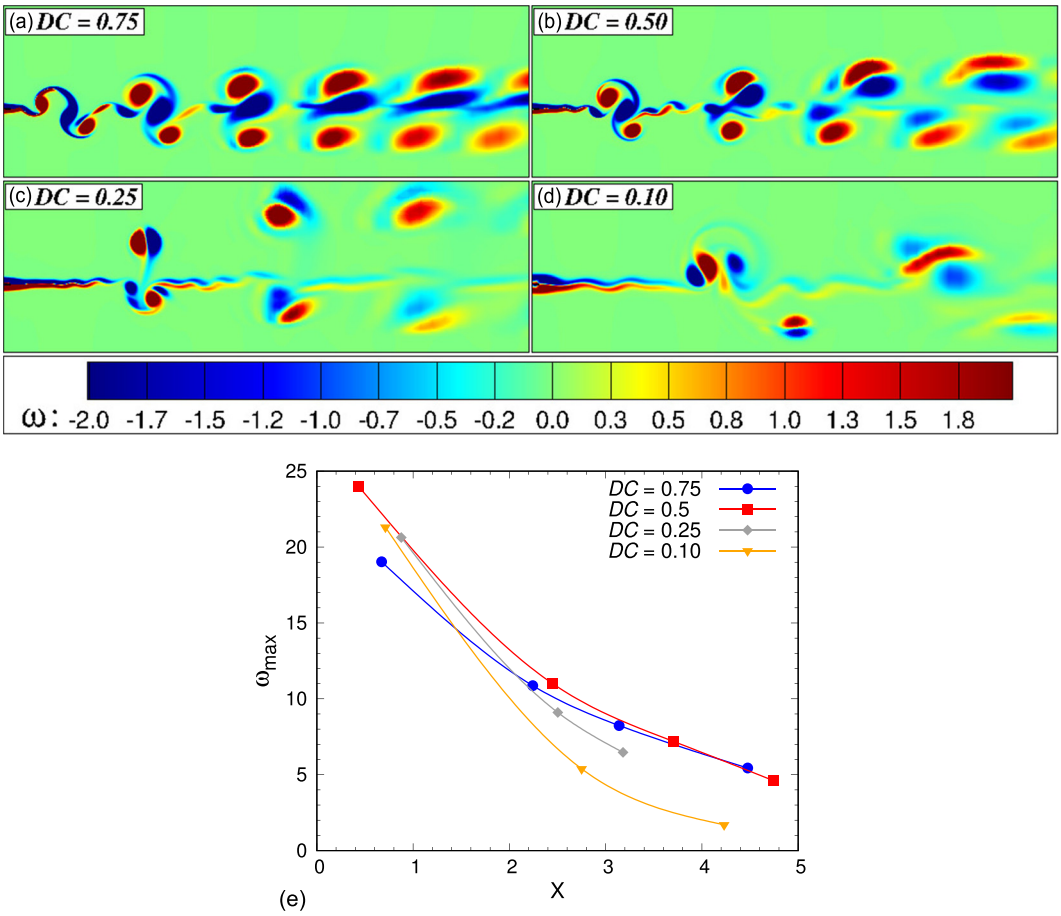

FIG. 11. For B&C swimming of a pitching hydrofoil ($\lambda^* \to \infty$) at $A_{max} = 0.1$, and $Re_f = 500$, effect of duty cycle DC on an instantaneous (a)–(d) vorticity contour and (e) streamwise variation of maximum vorticity ω_{max} of the shed vortex V^{CW}_{shed-2}.

that the transfer of larger momentum in the streamwise direction is much more efficient at a large Re_f and results in a greater energy savings, which is presented later in Sec. VIII.

C. Effect of duty cycle

The effect of duty cycle (DC)—associated with bringing the intermittent stopping of the swimming by adding a coast phase—on the instantaneous vortex street behind a pitching hydrofoil is shown in Fig. 11. Note that a smaller DC results in a larger coast-based intermittent stopping of the hydrofoil movements. The figure shows a dipole-based asymmetric RVK vortex street in the wake for $DC = 0.75$, the RVK together with a dipole-based FVK for $DC = 0.5$, and a much elongated shedding of the RVK and FVK vortex street for $DC = 0.25$ and 0.1. The difference in the various vortex streets is due to a difference in the time-averaged propulsion velocities $\bar{U}_P$ generated by the hydrofoil at different DC. At a large DC, the time during which the hydrofoil undulates is greater; thus, the time-averaged velocity and the streamwise jet-based surplus momentum in the wake will both be greater. For example, at $DC = 0.75$, the hydrofoil undulates 75% of its total B&C time; thus, the time-averaged velocity behind the foil is larger. Therefore, similar to the above discussed on the variation at a larger Re_f of 1500, the larger propulsive velocity at a larger DC stabilizes the newly formed vortex (formed by joining vortex V^{CW}_{shed-2} and V^{CW}_{shed-4}) and does not split into two, resulting in a dipole-based RVK with a separate CCW vortex at $DC = 0.75$. At very low DC values of 0.25 and 0.1, the propulsive velocity generated by the hydrofoil is very low and becomes comparable with the velocity of the lateral deviation of the dipole. As a result, the dipole travels downstream while rotating about its center, resulting in the much elongated vortex structures in the wake. Further, at $DC = 0.1$, the V^{CW}_{shed-2} breaks into two, which results in 5 different vortices in the wake [Fig. 11(d)].

Figure 11(e) shows that the maximum magnitude of vorticity of the vortex V^{CW}_{shed-2} for various DC is almost the same, and the downstream decay/dissipation of the shed vortices is similar for all the DC values. Figures 11(a)–11(d) also show that the rightward deviation of RVK vortex street increases with the decreasing DC up to 0.25 and decreases at $DC = 0.1$. The increase in lateral deviation is due to a decrease in time-averaged propulsive velocity $\bar{U}_P$, as discussed above. Thus, the number of observable vortices in the wake varies from three to five depending upon the DC of the B&C swimming.

VIII. PROPULSIVE PERFORMANCE: BURST-AND-COAST vs CONTINUOUS SWIMMING AND CONNECTION WITH NATURE

As discussed in Sec. V, the B&C swimming as compared to the continuous swimming leads to a decrease in the input power for the hydrofoil motion, along with a decrease in the propulsive velocity. The decrease in the input power leads to a decrease in the input energy while the decrease in the propulsion velocity leads to an increase in the time to travel the same distance "d" that is traveled with the continuous swimming. Thus, a comparative propulsion performance of the B&C and continuous swimming is presented here in terms of non-dimensional parameters as follows:

$$\begin{aligned} \%\text{Energy Savings} &= (1 - E_R) * 100\%, \\ \%\text{time-Enhancement} &= (T_R - 1) * 100\%, \\ \text{Effectiveness of B \& C swimming} &= \frac{\%\text{Energy Savings}}{\%\text{time-Enhancement}}, \end{aligned} \tag{15}$$

where E_R is the energy ratio and T_R is the time ratio, which are given as

$$\begin{aligned} E_R &= \frac{E_{b-c}}{E_{cont}} = \frac{\bar{C}_{P,in,b-c}\ \tau_{b-c}}{\bar{C}_{P,in,cont}\ \tau_{cont}} = \frac{\bar{C}_{P,in,b-c}\ /\bar{U}_{P,b-c}}{\bar{C}_{P,in,cont}\ /\bar{U}_{P,cont}}, \\ \text{and} \quad T_R &= \frac{\tau_{b-c}}{\tau_{cont}} = \frac{\bar{U}_{P,cont}}{\bar{U}_{P,b-c}}, \end{aligned} \tag{16}$$

where E is the input energy, $\bar{C}_{P,in}$ is the mean non-dimensional input power [Eq. (13)], and τ $(= D/\bar{U}_P)$ is the non-dimensional time required to cover the same non-dimensional distance D at the periodic state.

The variation of the various propulsive parameters for the B&C as compared to the continuous swimming is shown in Fig. 12. The effects of the wavelength λ^* of undulation (at $DC = 0.5$) and DC (at $\lambda^* = 0.8, 1.8,$ and ∞) are presented in the figure for various $Re_f = 50, 500,$ and 1500. With the increasing λ^* at various Re_f, Figs. 12(a) and 12(c) show an asymptotic increase in both %energy savings and effectiveness of the B&C compared to continuous swimming, while Fig. 12(b) shows an increase followed by an asymptotic decreasing trend of variation of the %time enhancement. With the increasing Re_f at a constant λ^*, the figure shows a decrease in the %time enhancement and an increase in the other comparative propulsive performance parameters. The shaded region in Fig. 12(c) shows the governing parametric values for which the effectiveness is greater than one, i.e., the %energy savings is more than the %time enhancement for the B&C as compared to the continuous swimming while traveling the same distance. The figure shows that a hydrofoil operating at a large value of λ^* (>3) and larger Re_f $(=1500)$ is effective for the B&C swimming as compared to the continuous swimming.

The larger wavelength λ^* of undulation corresponds to a smaller value of wavenumber $W(= C/\lambda = 1/\lambda^*)$, which is presented on the top x axis of Figs. 12(a)–12(c). The wavenumber W is shown here as it represents the muscle-induced flexibility of a fish that is seen to decrease with the increasing wavelength λ^* of undulation. The present result shows that the B&C swimming is effective at larger λ^* and supports the choice of B&C swimming by certain fish—chosen by the carangiform and thunniform fish but never chosen by the anguilliform fish as observed in nature. Note that the kinematics of carangiform and thunniform fish involve the pitching motion ($\lambda^* \to \infty$ or $W = 0$) of their caudal fin while that of the anguilliform fish involves a larger muscle-induced chordwise flexibility (larger W or smaller λ^*) based undulation of the whole body. Our numerical results on %energy savings = 43% for the pitching hydrofoil, which corresponds to $W = 0$ or $\lambda^* \to \infty$, at $Re_f = 1500$ [Fig. 12(a)] match closely with the energy savings = 45% that was reported experimentally for a live koi carp (carangiform) fish by Wu *et al.*[7]

With the decreasing duty cycle DC for various Re_f and λ^*, Fig. 12(d) shows an almost linear increase in the %energy savings (except a sharply increasing trend at $\lambda^* = 0.8$) while Fig. 12(e) shows a sharply increasing trend of variation of the %time enhancement. Thus, for a larger %energy savings as compared to the %time enhancement, the marked region for the effectiveness > 1 in Fig. 12(f) shows that B&C swimming is effective at an intermediate $DC = 0.75$ and 0.5. The figure shows that the $DC = 0.75$ is effective for intermediate $\lambda^* = 1.8$ as well as larger $\lambda^* \to \infty$ at high $Re_f = 1500$ and for high $\lambda^* \to \infty$ at low $Re_f = 50$; however, $DC = 0.5$ is effective only for the larger $\lambda^* \to \infty$ and high $Re_f = 1500$. These findings also support the observations of B&C swimming occurring only at the larger DC. For example, B&C swimming was reported for golden shiners fish at $DC \approx 0.7$[9] and for koi carp fish at $DC \approx 0.4$.[7] Furthermore, B&C swimming is mostly observed in the inertial range (larger Re_f) except at low $Re_f \approx 10$ by a larval zebrafish.[6]

IX. CONCLUSIONS

The present numerical study is on the self-propulsion of a NACA0012 hydrofoil, which is based on intermittent burst-and-coast (B&C) and continuous swimming modes as well as undulation and pitching swimming kinematics; these are the modes adopted by the body/tail of various BCF fish. Thus, the effect of the associated governing parameters—intermittency-based duty cycle DC $(= 0.1 - 1)$ for the swimming modes and wavelength λ^* $(= 0.8 - \infty)$ of undulation for the swimming kinematics—are studied here for the various frequency-based Reynolds number $Re_f (= 500 - 1500)$. The conclusions drawn from the present work are as follows:

1. Using the same swimming kinematics as continuous swimming during the burst phase and stationary during the coast phase, a B&C as compared to continuous swimming hydrofoil is found to result in a substantial reduction in input power along with a decrease in the propulsive velocity. However, for both the types of swimming, these parameters increase with the increasing wavelength λ^* of undulation or decreasing muscles-induced flexibility.
2. A swimming kinematics driven vortex–hydrofoil interaction dynamics is demonstrated to lead to a sequence of vortical events—stopping, starting and finally, shedding of vortices—in the near-wake region. The near wake vorticity dynamics is shown to lead to a difference in vortex street in the far-wake region—an asymmetric reverse von Karman (RVK) and forward von Karman (FVK) vortex streets for the B&C swimming as compared to the symmetric RVK street during the continuous swimming. The sequence of events for the process of vortex shedding is discussed, where the growth, stretching, and advection of the vortices get curtailed during the intermittent stopping of the B&C swimming hydrofoil.

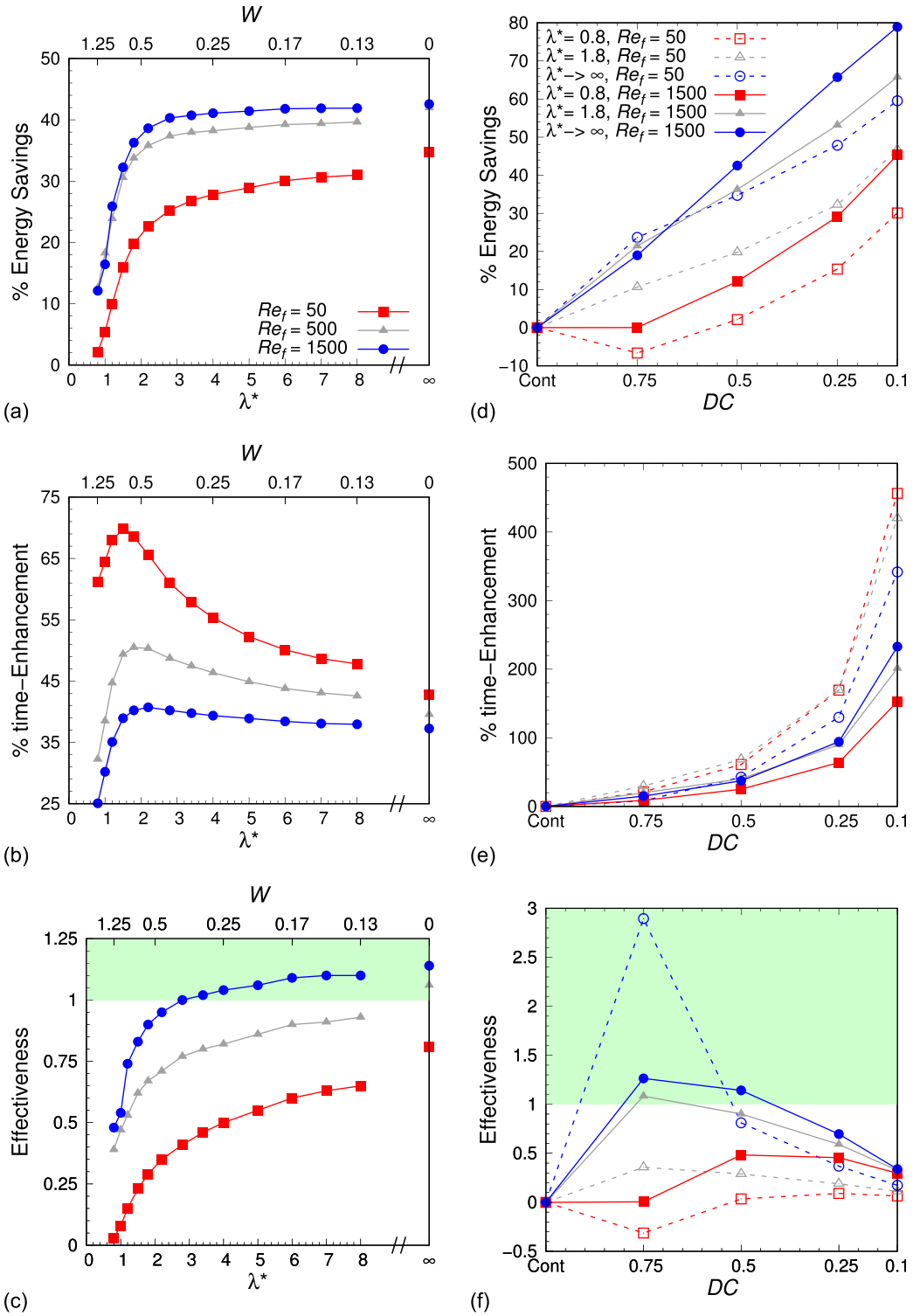

FIG. 12. Variation of (a and d) %energy savings, (b and e) %time enhancement and (c and f) effectiveness of B&C as compared to the continuous swimming, with (a)–(c) increasing wavelength λ^* (decreasing wavenumber $1/\lambda^*$) and (d)–(f) decreasing duty cycle *DC* of undulation at various Reynolds number Re_f. The subfigures of (a)–(c) are at $DC = 0.5$ and (d)–(f) are at $\lambda^* = 0.8, 1.8$, and ∞. The shaded region in subfigures (c) and (f) shows the cases with the values of effectiveness greater than one.

3. The size, strength, and number of the shed vortices in the far wake varies with the governing parameters. An increasing λ^* leads to the transition from undulation to pitching, and the size and strength of the shed vortices increase from three ($\lambda^* < 1.8$) to five (for $\lambda^* > 1.8$). The number of shed vortices reduces from four at $Re_f = 500$ to three at $Re_f = 1500$; and from five at $DC = 0.1$ to three at $DC = 0.75$.
4. Finally, for the B&C as compared to continuous swimming, the effect of the reduction in both input power and propulsive velocity is found to result in energy saving along with an increase in the travel time to cover a same distance by both the types of swimming. The energy saving increases with the increasing λ^*, DC and Re_f while the time enhancement decreases with the increasing DC and Re_f. An effectiveness of the B&C as compared to continuous swimming is defined, with the energy saving greater than the time enhancement, where the B&C is found to be effective for a larger λ^*, Re_f and DC. Thus, our result supports and explains why the B&C swimming is adopted by a carangiform and thunniform fish that mainly follows a larger-λ^*-based pitching swimming kinematics while it is not adopted by anguilliform fish which mainly follow a smaller-λ^*-based undulating swimming kinematics.

The present results are significant as they demonstrate several propulsive characteristics of B&C swimming and provide vorticity-dynamics-based fluid-dynamics reasons for its adoption only by a certain class of BCF fish in nature. Further, it fills the gap and helps us understand the difference in the number of shed vortices reported in the literature for the B&C swimming. Although the B&C swimming-based energy saving has been reported, its correlation with the enhancement in the travel time as well as its effectiveness is presented here for the first time.

DATA AVAILABILITY

The data that support the findings of this study are available from the corresponding author upon reasonable request.

REFERENCES

[1]M. Sfakiotakis, D. M. Lane, and J. B. C. Davies, "Review of fish swimming modes for aquatic locomotion," IEEE J. Ocean. Eng. **24**, 237–252 (1999).
[2]C. Breder, "The locomotion of fishes," Zoologica **4**, 159–297 (1926).
[3]J. Magnusson, W. Hoar, and D. Randall, "Locomotion by scombroid fishes: Hydromechanics, morphology, and behaviour," Fish Physiol. **7**, 240–315 (1978).
[4]D. Weihs, "Energetic advantages of burst swimming of fish," J. Theor. Biol. **48**, 215–229 (1974).
[5]J. Videler and D. Weihs, "Energetic advantages of burst-and-coast swimming of fish at high speeds," J. Exp. Biol. **97**, 169–178 (1982).
[6]U. Muller, E. Stamhuis, and J. Videler, "Hydrodynamics of unsteady fish swimming and the effects of body size: Comparing the flow fields of fish larvae and adults," J. Exp. Biol. **203**, 193–206 (2000).
[7]G. Wu, Y. Yang, and L. Zeng, "Kinematics, hydrodynamics and energetic advantages of burst-and-coast swimming of koi carps (*Cyprinus carpio koi*)," J. Exp. Biol. **210**, 2181–2191 (2007).
[8]D. L. Kramer and R. L. McLaughlin, "The behavioral ecology of intermittent locomotion," Am. Zool. **41**, 137–153 (2001).
[9]F. E. Fish, J. F. Fegely, and C. J. Xanthopoulos, "Burst-and-coast swimming in schooling fish (NOTEMIGONUS CRYSOLEUCAS) with implications for energy economy," Comp. Biochem. Physiol. B **100**, 633–637 (1991).
[10]M. J. Lighthill, "Large-amplitude elongated-body theory of fish locomotion," Proc. R. Soc. London B **179**, 125–138 (1971).
[11]R. Bainbridge, "Caudal fin and body movement in the propulsion of some fish," J. Exp. Biol. **40**, 23–56 (1963).
[12]L. C. Rome and R. M. Alexander, "The influence of temperature on muscle velocity and sustained performance in swimming carp," J. Exp. Biol. **154**, 163–178 (1990).
[13]G. Iosilevskii, "Locomotion of neutrally buoyant fish with flexible caudal fin," J. Theor. Biol. **399**, 159–165 (2016).
[14]R. Blake, "Functional design and burst-and-coast swimming in fishes," Can. J. Zool. **61**, 2491–2494 (1983).
[15]M. Chung, "On burst-and-coast swimming performance in fish-like locomotion," Bioinspiration Biomimetics **4**, 036001 (2009).
[16]U. Ehrenstein and C. Eloy, "Skin friction on a moving wall and its implications for swimming animals," J. Fluid Mech. **718**, 321–346 (2013).
[17]U. Ehrenstein, M. Marquillie, and C. Eloy, "Skin friction on a flapping plate in uniform flow," Philos. Trans. R. Soc. A **372**, 20130345 (2014).
[18]E. Akoz and K. W. Moored, "Unsteady propulsion by an intermittent swimming gait," J. Fluid Mech. **834**, 149–172 (2018).
[19]D. Floryan, T. Van Buren, and A. J. Smits, "Forces and energetics of intermittent swimming," Acta Mech. Sin. **33**, 725–732 (2017).
[20]J. C. Liao, "Swimming in needlefish (Belonidae): Anguilliform locomotion with fins," J. Exp. Biol. **205**, 2875–2884 (2002).
[21]N. Thekkethil, A. Sharma, and A. Agrawal, "Unified hydrodynamics study for various types of fishes-like undulating rigid hydrofoil in a free stream flow," Phys. Fluids **30**, 077107 (2018).
[22]F. Fish and G. V. Lauder, "Passive and active flow control by swimming fishes and mammals," Annu. Rev. Fluid Mech. **38**, 193–224 (2006).
[23]S. Kern and P. Koumoutsakos, "Simulations of optimized anguilliform swimming," J. Exp. Biol. **209**, 4841–4857 (2006).
[24]X. Chang, L. Zhang, and X. He, "Numerical study of the thunniform mode of fish swimming with different Reynolds number and caudal fin shape," Comput. Fluids **68**, 54–70 (2012).
[25]M. Gazzola, M. Argentina, and L. Mahadevan, "Scaling macroscopic aquatic locomotion," Nat. Phys. **10**, 758–761 (2014).
[26]J. Videler and C. Wardle, "Fish swimming stride by stride: Speed limits and endurance," Rev. Fish Biol. Fish. **1**, 23–40 (1991).
[27]N. Thekkethil, A. Sharma, and A. Agrawal, "Self-propulsion of fishes-like undulating hydrofoil: A unified kinematics based unsteady hydrodynamics study," J. Fluids Struct. **93**, 102875 (2020).
[28]A. Leroyer and M. Visonneau, "Numerical methods for RANSE simulations of a self-propelled fish-like body," J. Fluids Struct. **20**, 975–991 (2005).
[29]I. Borazjani and F. Sotiropoulos, "On the role of form and kinematics on the hydrodynamics of self-propelled body/caudal fin swimming," J. Exp. Biol. **213**, 89–107 (2010).
[30]J. Carling, T. L. Williams, and G. Bowtell, "Self-propelled anguilliform swimming: Simultaneous solution of the two-dimensional Navier-Stokes equations and Newton's laws of motion," J. Exp. Biol. **201**, 3143–3166 (1998).
[31]D. Kim and H. Choi, "Immersed boundary method for flow around an arbitrarily moving body," J. Comput. Phys. **212**, 662–680 (2006).
[32]M. Beddhu, L. K. Taylor, and D. L. Whitfield, "Strong conservative form of the incompressible Navier–Stokes equations in a rotating frame with a solution procedure," J. Comput. Phys. **128**, 427–437 (1996).
[33]N. Thekkethil and A. Sharma, "Level set function–based immersed interface method and benchmark solutions for fluid flexible-structure interaction," Int. J. Numer. Methods Fluids **91**, 134–157 (2019).
[34]B. Eaton, "Analysis of laminar vortex shedding behind a circular cylinder by computer-aided flow visualization," J. Fluid Mech. **180**, 117–145 (1987).